FEATURE ARTICLE

ChemComm
www.rsc.org/chemcomm

High-resolution transmission electron microscopy: the ultimate nanoanalytical technique†‡

John Meurig Thomas*[ab] and Paul A. Midgley[a]

[a] *Department of Materials Science and Metallurgy, University of Cambridge, New Museums Site, Pembroke Street, Cambridge CB2 3QZ. E-mail: jmt@ri.ac.uk; Fax: 01223 334567; Tel: 01223 334467*

[b] *Davy Faraday Research Laboratory, The Royal Institution of Great Britain, 21 Albemarle Street, London W1S 4BS. E-mail: jmt@ri.ac.uk; Fax: 020 7670 2958; Tel: 020 7670 2928*

Received (in Cambridge, UK) 1st December 2003, Accepted 16th February 2004

To be able to determine the elemental composition and morphology of individual nanoparticles consisting of no more than a dozen or so atoms that weigh a few zeptograms (10^{-21} g) is but one of the attainments of modern electron microscopy. With slightly larger specimens (embracing a few unit cells of the structure) their symmetry, crystallographic phase, unit-cell dimension, chemical composition and often the valence state (from parallel electron spectroscopic measurements) of the constituent atoms may also be determined using a scanning beam of electrons of *ca.* 0.5 nm diameter. Nowadays electron crystallography, which treats the digital data of electron diffraction (ED) and high-resolution transmission electron microscope (HRTEM) images of minute (*ca.* 10^{-18}g) specimens in a quantitatively rigorous manner, solves hitherto unknown structures just as X-ray diffraction does with bulk single crystals. In addition, electron tomography (see cover photograph and its animation) enables a three-dimensional picture of the internal structure of minute objects, such as nanocatalysts in a single pore, as well as structural faults such as micro-fissures, to be constructed with a resolution of 1 nm from an angular series of two-dimensional (projected) images. Very recently (since this article was first written) a new meaning has been given to electron crystallography as a result of the spatio-temporal resolution of surface phenomena achieved on a femtosecond timescale.

Sir John Meurig Thomas is a solid-state and surface chemist who is renowned for his work on the design of new catalysts and their in situ characterisation. Formerly he was Head of the Department of Physical Chemistry, Cambridge and Director of the Royal Institution. He has had many honours for his work on catalysis and was the first recipient of the American Chemical Society Award for Creative Research in Homogeneous and Heterogeneous Catalysis in 1999.

Paul Midgley is a Reader in Electron Microscopy and Director of the Electron Microscopy Facility at the Department of Materials Science and Metallurgy in Cambridge. He studied Physics at the H.H. Wills Physics Laboratory at the University of Bristol, receiving his PhD in 1991 for electron microscopy studies of high Tc superconductors. He then held two Research Fellowships, the first funded by The Royal Commission for The Exhibition of 1851, the second by The Royal Society. He moved to Cambridge in 1997. He has studied a wide variety of materials by electron microscopy and developed a number of novel electron microscopy techniques. He and his research group have developed new analytical techniques using energy-filtered TEM, STEM and electron holography and applied these to materials systems at the nanometre level. Recently, he has worked on the development of electron tomography using a new STEM-based approach that has wide applicability in the physical sciences.

Introduction

HRTEM has, since the early 1970s,[1–3] been of growing importance in the armoury of solid-state chemists and earth scientists, and especially of those who prepare and study the chemistry of new (condensed-matter) materials. Advances in instrumentation, encompassing high-precision electron-optical lenses, digital electronics and general detector technology (particularly slow-scan charge-coupled devices) in the intervening years has made the electron microscope with its parallel electron spectroscopic and imaging-filter facilities a well-nigh indispensable tool in the armamentarium of the materials-oriented chemist, ceramicist, catalyst scientist, device engineer, nanotechnologist, earth scientist and geochemist.

This article outlines some of the key developments and concentrates mainly on illustrative examples of how electron-optical methods, by uncovering unexpected new families of structures, concepts and mechanisms, have transformed the landscape of solid-state and materials chemistry. Adequate introductory accounts of the actual techniques and underlying principles of HRTEM, its scanning transmission (HRSTEM) analogue,[4] as well as electron-energy-loss spectroscopy (EELS)[5] studied using an electron microscope, are available. Here, we shall focus principally on application and the nature of the consequential advances in our chemical knowledge.

Selected area electron diffraction (SAED)

Even the most beam-sensitive of materials—usually these are organic molecular crystals which tend to carbonize under electron-beam irradiation—may readily be examined by low-dose and selected area diffraction either by conventional TEM or by STEM instruments.

When, for example, specimens of anthracene are subject to stress, it transpires, from microluminescent and microdiffraction measurements, that the stable monoclinic phase is converted to a new crystallographic triclinic one.[6] From the resulting SAED patterns both the unit-cell dimensions and the symmetry of the new phase may be readily retrieved. By then using appropriate atom–atom potentials as well as employing standard computational methods of the kind pioneered by Kitaigorodski on this new phase, the precise unit-cell structure may be determined, and so also may its phonon spectrum.[7] (Subsequent neutron scattering experiments have confirmed the veracity of the predicted phonon modes). The new structure also reveals why stressed samples of anthracene readily form photo-dimers (9,10 di-paraanthracene) when exposed to u.v. light, since, as expected from well-known topochemical

---

† Electronic supplementary information (ESI) available: an animation of the reconstruction shown in the graphical abstract and Fig. 25 reveals the presence of Pt/Ru nanoparticles within a single mesopore. See http://www.rsc.org/suppdata/cc/b3/b315513g/

‡ An updated version of the Pitzer Lecture given by J. M. Thomas at the University of California, Berkeley, 1988 entitled “Electron Microscopy and the Chemist” and his plenary lecture at the joint ACS, RSC, RSC (Canada), Bloomington, Indiana in 1982 on “Inorganic Chemistry: Towards the 21st Century”—see ref. 5

DOI: 10.1039/b315513g

principles,[8] two adjacent molecules of the anthracene are in favourable juxtaposition for photodimerization to ensue.

At low temperature (below 120 K), the excimeric behaviour of pyrene exhibits a distinct change from that of the room-temperature stable polymorph. Selected-area electron diffraction (taken using a liquid nitrogen-cooled specimen stage) again reveals a new phase, the precise crystallographic structure of which may be determined by appropriate atom–atom computation.

In the identification of structural imperfections such as line defects (dislocations) or coincidence and twin boundaries, electron microscopy is indispensable. From a combination of SAED patterns and images taken either in dark field (DF)—*i.e.* with only diffracted beams[5]—such fundamental solid-state properties as Burgers vectors (which essentially define a dislocation), slip planes and stacking faults (and their associated energies) may be determined. All this proved crucial in elucidating the role of structural imperfections in the reactivity, photochemistry and photophysics of the organic solid state.[9] For example, it was shown that, at stacking faults, two juxtaposed monomers are brought into favourable topochemical orientation so as to photodimerize when the solid is exposed to u.v. light.

SAED patterns (of specimens that have 10^5 to 10^8 unit cells) are invaluable in detecting superlattices (or supermeshes) that signify either regular distortion, or recurrent intergrowths, or especially the ordering of anion vacancies—which is the case in a wide range of non-stoichiometric oxides. In the so-called defective perovskites—materials with formulae ABO_{3-x}, where $0 < x < 0.5$, many new, well-defined, intermediate crystallographic phases were identified by SAED[10] (Fig. 1). With $CaMnO_{3-x}$, for example, five distinct compositions ($CaMnO_{2.50}$, $CaMnO_{2.556}$, $CaMnO_{2.667}$, $CaMnO_{2.75}$ and $CaMnO_{2.80}$) with highly ordered oxygen vacancies were identified. These subtly different, grossly non-stoichiometric oxides are readily interconverted one to the other when they are used as selective oxidation catalysts for alkanes or alkenes. The ease with which oxygen vacancies may be created, when a hydrocarbon uproots an oxide ion from the solid, or when the vacancies are filled up by the incorporation of gaseous oxygen (the oxidant), explains why so many perovskitic solid oxides, as well as several other metal oxides of different structural types, such as the large family of bismuth molybdates, are very good so-called Mars and van Krevelen oxidation catalysts, where the oxygen of the solid catalyst is used, as it were sacrificially, to oxidise the hydrocarbon, and where the anion vacancies thus formed are made good by incorporation of gaseous O_2.

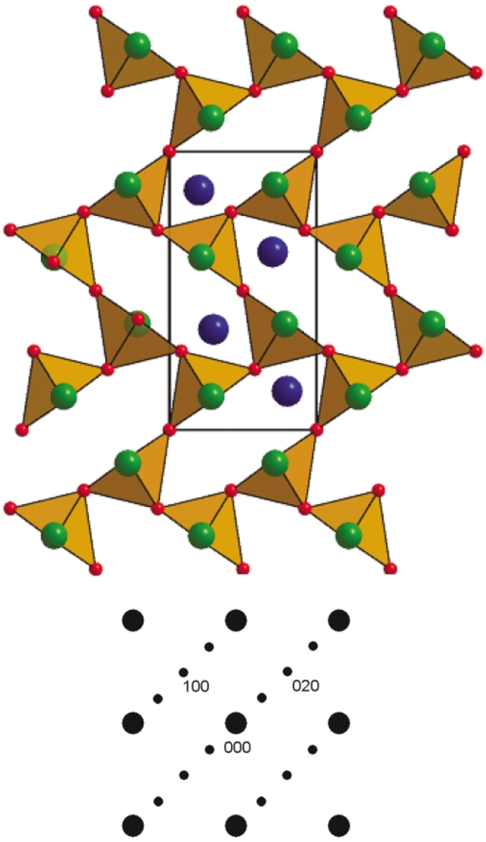

Fig. 1 Selected-area electron diffraction (SAED) establishes that the grossly non-stoichiometric perovskitic oxide $CaMnO_{3-x}$ ($0 < x < 0.5$) takes up numerous distinct structures in which the oxygen (anion) vacancies are ordered. One of the three structures, and the corresponding SAED pattern, taken up by $CaMnO_{2.5}$ is shown here.[10] Blue = calcium, red = oxygen, green = manganese. The unit cell is outlined.

Shortly after SAED patterns were found, in the early 1970s, to be readily recordable, they transformed the inorganic chemist's knowledge of the nature of gross non-stoichiometry whilst simultaneously revealing the existence of hitherto unknown families of so-called "homologous" structures. Thus CrO_2, which has the rutile structure, when rendered non-stoichiometric by reduction, forms new structures Cr_nO_{2n-1} (with $n = 4$ to 6),[11] similar to those reported for TiO_2, which also exhibits a Ti_nO_{2n-1} family of homologous structures[11] (see also Table 1).

In examining the ternary oxides derived from Bi_2O_3 (*i.e.* the systems Bi_2O_3–Nb_2O_5, Bi_2O_3–Ta_2O_5, Bi_2O_3–MoO_3, Bi_2O_3–WO_3 and Bi_2O_3–V_2O_5), one of us found, from the superlattices signified in the relevant SAED patterns (Fig. 2), numerous new families of ordered phases based on the fluorite structure.[12] The high-temperature stable form δ-Bi_2O_3 is itself a defective fluorite structure rich in anion vacancies, and best described as $Bi_2O_3\square$, where $\square$ represents an oxygen anion vacancy per formula unit of a 'double fluorite' (Ca_2F_4) repeat. Our electron diffraction patterns reveal the efficacy of the fluorite structure as a vehicle for accommodating wide ranges of compositions derived from Bi_2O_3. It seems that incorporation of foreign metal ions with higher valences (than Bi) stabilize the high-temperature δ-Bi_2O_3 structure at lower temperatures. Indeed, for the Bi_2O_3–MoO_3 system, which are highly effective selective oxidation catalysts, fluorite-derived structures are taken up over the entire compositional range.[13]

The mere appearance of a SAED pattern can alone signify a highly significant structural feature. The classic example is the discovery of quasi-crystals, where five-fold symmetry, previously thought not to be feasible in crystalline solids, was unambiguously discovered by electron microscopy. Less dramatic, but quite important in the ever-growing realm of organic conductors, was the detection of amorphous phases in evaporated specimens of polynuclear aromatic hydrocarbons by low-temperature electron diffraction.

Convergent beam electron diffraction (CBED)

A complementary, and sometimes more powerful, mode of electron diffraction, is convergent beam electron diffraction (CBED) in which a focused beam, often just a few nm in diameter, is used to select the area from which the diffraction pattern is formed. The high convergence angle gives rise to discs rather than spots in the back focal plane of the objective lens (diffraction plane) and the contrast seen within each disc can be regarded as a 'map' of diffracted intensity as a function of orientation for each set of planes (reflections). It is this detail that gives CBED its power to elucidate the symmetry of crystals to map strain and orientation and to enable the structure factors to be determined with such accuracy that maps of bonding charge density can be calculated[14] (see Fig. 3). However, perhaps its most important role is to allow the determination of the atomic positions of crystals that cannot be determined using any other technique, partly because of their small volume fraction of a multi-phasic specimen or because of their metastability. Take the case of the phase in the Au–Sn system formed by reacting elemental Au and Sn *in situ* in the electron microscope.[15] A new tetragonal form of $AuSn_4$ was determined using diffraction patterns acquired by CBED, see Fig. 4. The heavy Au and Sn atoms prohibited the use of low order reflections for the elucidation of the structures as their intensities suffer enormously from multiple scattering effects. However, reflections in the so-

Table 1 Selected examples of chemical, structural and mechanistic insights and discoveries gained by transmission electron microscopy

Structure, phenomenon, discovery or mechanism	Example	Reference
A. Determination of new structure by:		
(i) Electron crystallography	(a) Microporous (zeolite solid) MCM-48	73
	(b) Mesoporous silica SBA-6	74
(ii) The 'multi-slice' approach	(a) CoALPO-36, $Bi_2(Mo,W)_{12}O_{35}$ each of which are selective oxidation catalysts	75
	(b) The mineral rhodizite $(K_{0.44}Cs_{0.76}Rb_{0.07})B_{11.3}Be_{4.5}Al_4O_{28}$	32
(iii) Convergent beam electron diffraction	(a) $AuSn_4$	14
	(b) AuGeAs	76
(iv) Selected area electron diffraction	(a) Metastable phases of organic molecular crystals (anthracene, pyrene)	6,7
	(b) Peroskitic oxides with ordered anion vacancies; $CaMnO_{2.5}$, $CaMnO_{2.75}$	10
	(c) Cr_nO_{2n-1} (n = 4,5,6…)	11
	(d) Quasicrystals with 5-fold symmetry	77
B. Incommensurate structures		
(i) Three-dimensional situations	(a) Au–Mg alloys	78
	(b) Au–Zn alloys	79
	(c) Au–Mn alloys	80
(ii) Two-dimensional situations	Graphite intercalates; transition metal dichalcogenides exhibiting charge-density waves (CDWs)	81
(iii) One-dimensional situations	Guest species inside channel (tube) hosts, metal halides in carbon nanotubes	50
C. Chemical insights		
	All these ((i) to (v) inclusive) are feasible using EELS: For example:	
(i) Chemical compositions	(a) Compositions of oxides, halides, chalcogennides, nitrides and carbides (from K-, L- or M-edge peaks)	55
(ii) Valence states of elements	(b) Plasmon spectra yield thicknesses and sometimes element identification (or bonding clues, as with π or σ plasmons in carbonaceous solids)	55
(iii) Element and thickness mapping; identification of trace elements in highly localised regions	(c) Detection of elemental nitrogen in platelets inside certain diamond samples.	82
(iv) Indications of tetrahedral or octahedral environments around light elements	(d) Proof that in lithium carbide there are ions	83
	(e) Proof that BeO_4 and AlO_6 polyhedra exist in the mineral rhodizite	59
(v) Element-selective single atom imaging	(f) Gd distribution in Gd@C_{82}	69
D. Morphology and topography		
(i) Dynamic shape changes of nanoparticles	(a) Cu particles on ZnO supports (catalysts for methanol synthesis)	69
(ii) Estimates of magnitude of diffusivities of particles at surface	(b) Monatomic steps and single vacancy concentrations in layered minerals	2,66
(iii) Topography of surfaces (by decoration)	(c) Spiral growth (and oxidation) features at mineral surfaces	2
(iv) Tomographic analysis, yielding location and distribution of nanoparticles inside nanoporous hosts	(d) Morphology and distribution of nanoparticle catalysts ($Ru_{10}Pt_2$ on silica)	54,63
E. Coherent intergrowths and the discovery of new families of structures		
(i) Magneli phases exhibited in the non-stoichiometric oxides of WO_{3-x}, MoO_{3-x}, ReO_{3-x}	(a) HRTEM showed that families such as W_nO_{3n-1}, W_nO_{3n-2} with n ranging from 6 to 20 consist of crystallographic shear (CS) planes at which a strip of oxide has edge-sharing rather than the normal face-sharing WO_6 octahedra. The larger the value of n the greater the separation of CS planes.	84
(ii) Crystallographic shear (CS) planes in non-stoichiometric TiO_2, VO_2 and CrO_2, typically TiO_x where $1.75 \le x \le 1.88$.	(b) HRTEM revealed CS planes where the normal edge-sharing of octahedra becomes face-sharing. Structure best thought of as Ti_nO_{2n-1} (n ranges from 4 to 9) and Cr_nO_{2n-1} (n = 4 to 6)	11
(iii) Block structures formed in certain ternary oxides (*e.g.* Nb_2O_5–WO_3)	(c) HRTEM shows these to be two families of intersecting CS planes	17
(iv) Infinitely adaptive structures occur within certain compositional structural extremes where a given composition has associated with it its own unique structure (as in the system Ta_2O_5–WO_3)	(d) This phenomenon was discovered by HRTEM	85
(v) Aurivillius phases: $(Bi_2O_2)^{2+}(A_{m-1}B_mO_{3m+1})^{2-}$	(e) Direct proof of the occurrence of this homologous series	21
(vi) A 'rotation-fault' within the corner-sharing WO_3 structure yields the tetragonal tungsten bronze structure.	(f) This happens in the system $4Nb_2O_5{\cdot}9WO_3$ and was discovered by HRTEM	86
(vii) Coherent intergrowths in zeolites.		
Two, unusually closely related structures form a coherent boundary. This may be regular and recurrent, or irregular. In the former case a 'new' structure results; in the latter, it is best to regard the situation in which one structure occurs irregularly within another, although a separate name may have already been given to the irregularly intergrown structures (*e.g.* ZSM-20)	(g) ECR-1 is seen, by HRTEM, to be a regular coherent intergrowth of sub-unit cell slabs of mazzite and morderite. Likewise in ZSM-23 there is a regular intergrowth of theta-1 and its twinned form.	37,38

Table 1 cont:

Structure, phenomenon, discovery or mechanism	Example	Reference
	The large family of so-called ABC-6 zeolites may be regarded as having been assembled architecturally from individual struts (thickness 2.6 Å) consisting of corner-sharing SiO_4^{4-} and AlO_4^{5-} tetrahedra. Offretite, erionite, chabazite and gmelinite are best envisaged in this way.	39
(viii) Coherent intergrowths of triple-chain, quadruple-chain and hexuple-chains (or corner-sharing SiO_4 tetrahedra) occur in mineral samples of amphiboles (which are double-chain structures)	(h) ZSM-20 and ZSM-3 are irregular intergrowths ofZSM-5 and ZSM-11.	87
	Pyroxenoids, a silicate family consisting of individual chains of SiO_4^{4-} tetrahedra, general formula $MSiO_3$ (M = Ca^{3+}, Mn^{2+}, Fe^{2+}…)	22
	(i) A class of recurrent intergrowths is formed when slabs of WO_3 coherent with strips of hexagonal tungsten oxide bronzes (HTB); they have large periodicities and are examples of modulated structures.	88
F. Surface and interface structures		
(i) HRTEM combined with X-ray emission (or other methods of elemental analyses) on a highly localised scale, reveals that surface structure and composition of complex oxides are often very different from those of the bulk phase.	(a) La_2CuO_4 at its exterior surface is essentially La_2O_3.	34
	(b) $SrTiO_3$ is more akin to TiO_2 at its (001) surface.	89
(ii) Coincidence boundaries, formed by a rotational twist between one part of a crystal and another, yield unusual interface structures.	(c) The $\surd 13.\surd 13$. R32.2° coincidence boundary in zeolite-L diminishes the diffusivity of molecules through the structures.	40
G. Facile interconversion of one structure into another		
(i) Martensitic transformation; induced by stress, in organic molecular crystals	(a) 1,8 dichloro-9 methylanthracene undergoes facile martensitic transformation, readily identified by SAED.	90
(ii) Conversion of one intercalate 'stage' into another by slight change of conditions. (An *n*th stage graphite intercalate has guest species accommodated every *n*th interlamellar space. HRTEM readily 'sees' *n*th, $n-1$th, $n-2$th *etc.* stages in such intercalates.)	(b) HRTEM shows that co-existent *n*th, $n-1$th, $n-2$th stages occur within one crystallite, thereby facilitating growth (or depletion) of one stage as a result of change of chemical driving force.	91

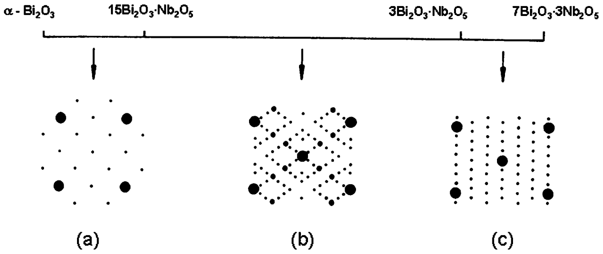

Fig. 2 SAED reveals that, in the solid solutions formed within the compositional extremes of Bi_2O_3 and $7Bi_2O_3.3Nb_2O_5$ three distinct ordered phases (designated Types I, II and III) exist. Schematic SAED (reciprocal lattice) patterns of these three fluorite-derived phases are shown: (a) Type I, down the [100] zone axis; (b) Type II, down [110]; and (c) Type III down [110]. In each case the reciprocal lattice points of the fluorite structure are shown as large filled circles. Reprinted with permission from *J. Phys. Chem.*, 1987, **91**, 512. Copyright 1987 American Chemical Society.[12]

called high-order Laue zones (HOLZ) can be treated in what is termed a quasi-kinematic way enabling conventional X-ray analysis to be performed on electron diffraction data.

High-resolution transmission electron microscopy (HRTEM)

It was also apparent in the 1970s that the point-to-point resolution of commercially available electron microscopes was already good enough to retrieve novel structural information from silicates, from graphite and its intercalates,[16,17] and from certain other minerals and solids of geochemical relevance.[18] Most of the interesting minerals, whose structures were then unknown, were microcrystalline (particle dimensions of 1 μm or less) and too small to be amenable to structure determination by single-crystal X-ray methods.[17,18] Moreover, many minerals, especially the microporous zeolites, exhibit a marked tendency to form intergrowths with closely similar structures.[19,20] These intergrowths are sometimes isolated, sometimes recurrent and frequently non-recurrent, thus complicating (often to the intractable limit) the resulting X-ray diffraction patterns.[21] Whereas X-ray based methods had yielded a

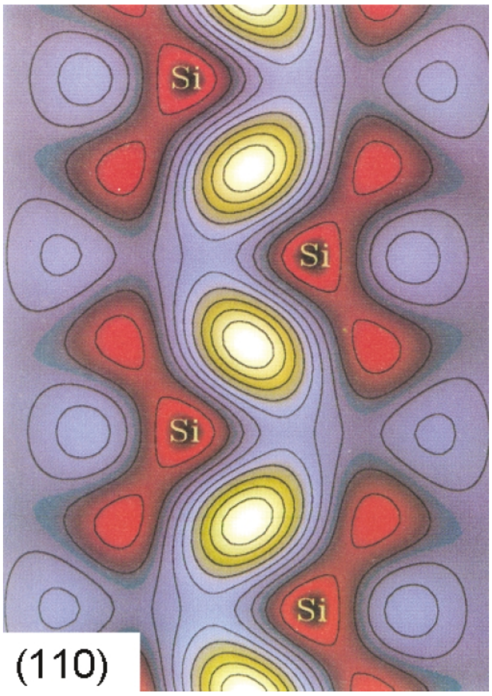

Fig. 3 (110) slice of bond-charge-density in silicon, reconstructed from a best-fit match to zone axis CBED pattern. The charge density map is determined by taking the Fourier transform of the difference between experimentally determined structure factors and those calculated assuming neutral atoms. The black and red areas show regions of electron deficiency, the white and yellow areas show electron excess (*i.e.* the chemical bond).[14]

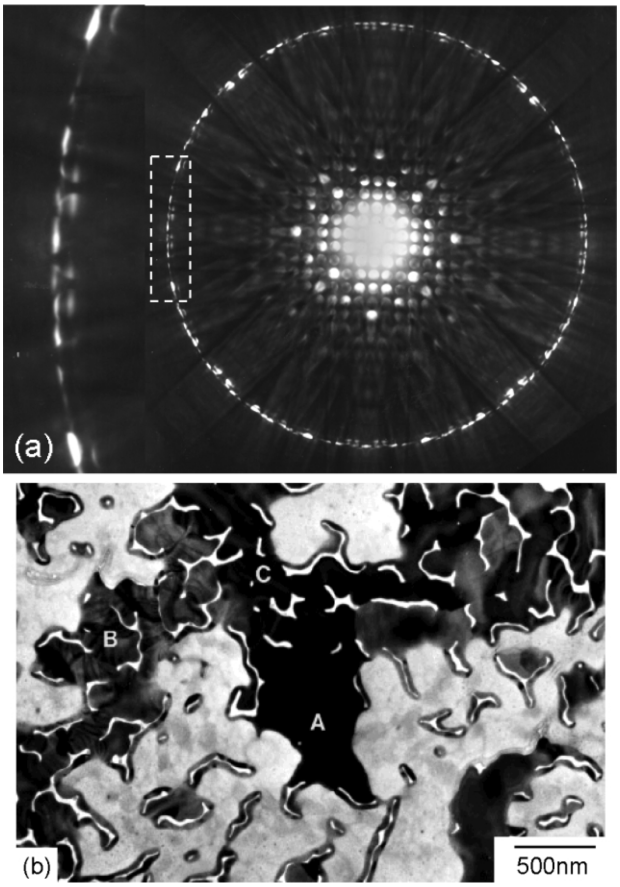

Fig. 4 (a) CBED pattern recorded at 150 kV parallel to the [001] zone axis of a new tetragonal $AuSn_4$ phase. The enlargement shows a symmetry-independent sector of the HOLZ ring, showing two excess lines (branches) within the CBED disks, the inner branch corresponds to a Bloch state sitting on the Au atoms, the outer branch on both Au and Sn (see text). The outer branch was used to determine the positions of the Sn atoms to 1 part in 200;[15] (b) the corresponding bright-field electron microscopic image where the letter A marks the metastable phase. Reprinted from *J. Solid State Chem.*, **124**, P. A. Midgley, M. W. Sleight and R. Vincent, "The structure of a metastable Au-Sn phase determined by convergent beam electron diffraction", p. 132, Copyright 1996, with permission from Elsevier.

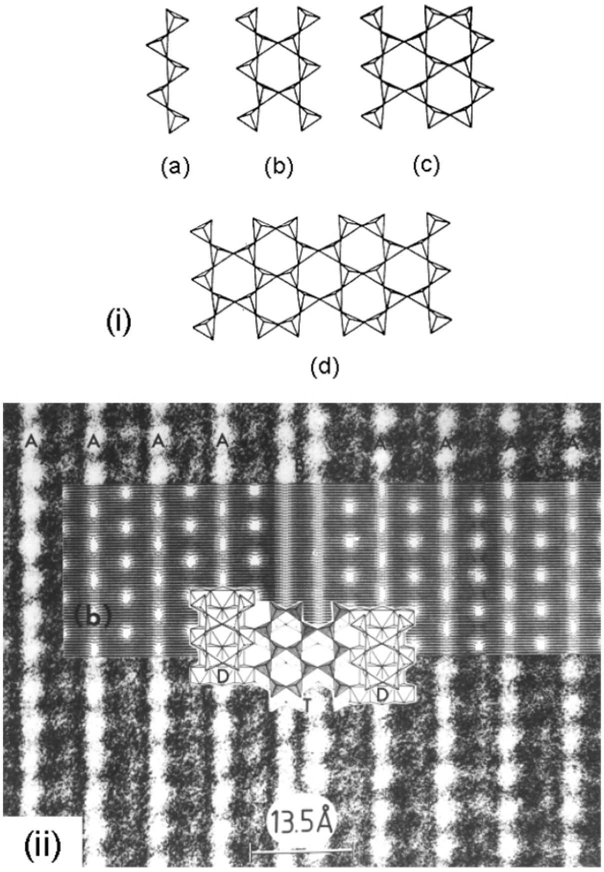

Fig. 5 (i) (a) Single-chain (pyroxene), (b) double-chain (amphibole), along with the triple (c) and sextuple (d) chains which, together with other multiply-linked and intergrown structures have been revealed (in real space) by HRTEM (images of the type shown in (ii)[23]); (ii) HRTEM images (a) together with the computed image (b) of a nephrite jade sample (from Zimbabwe, idealized formula $Ca_2Mg_5(Si_4O_{11})_2(OH)_2$). Note that the double chains (D) give rise to bright channels (A), whereas triple-chain infractions (T) give rise to two adjacent white channels (B) in the HRTEM image.[23] Reproduced with permission from The Royal Society of Chemistry.

good deal of ambiguous (at best) information concerning, for example, the spatial character of polytypic intergrowths in chain silicates (of the so-called pyroxenoid family, general formula $ASiO_3$ with A = Ca^{2+}, Mg^{2+}, Fe^{2+} and Mn^{2+}, such as wollastonite, rhodonite and pyroxmangite), HRTEM yielded precise and unambiguous information.[22]

Likewise, HRTEM studies of nephrite jade (an amphibole, the backbone of which has connected two parallel chains of corner-sharing SiO_4 tetrahedral) and jadeite (a pyroxene, with just a single chain of corner-sharing tetrahedraz) revealed, for the first time, that triple-chains and quadruple chains (even hexuple-chains) could exist in nature, as summarised in Fig. 5.[23] In addition, by synthesising "nominal" pyroxenes (such as $(Ca,Sr)(Si,Ge)O_3$), altogether new and totally unexpected types of structures, such as 'ring-chain' intergrowths were discovered.[24] And when, in the late 1970s, energy-dispersive, solid-state X-ray detectors could be attached to high-resolution microscopes, a new era began in structure–composition relationships in solid state chemistry, ceramics and mineralogy. It became possible, for example, to unravel the hitherto perplexing structure–composition relationships of the serpentine minerals general formula $Mg_3Si_2O_5(OH)_4$ (embracing antigorite, chrysotile and lizardite).[25] HRTEM, along with simultaneous energy dispersive analysis of the emitted X-rays (Fig. 6), unequivocally established that chrysotile and antigorite are polymorphs, with each being free of aluminium, and that lizardite has aluminium in both octahedral and tetrahedral coordination.[25]

With the continuing improvements in performance of electron microscopes from the early 1980s onwards, the resolution of atomic planes of separation less than 2 Å became possible. But there are both fundamental and practical difficulties that demand great caution in the interpretation of high-resolution (real-space) images. The strong interaction between electrons and atoms lead to multiple scattering (*i.e.* so-called dynamical phenomena), which are quite complex, though computable. In addition, electron lenses always contribute some degree of spherical aberration, and image information is also limited by the chromatic aberration created by energy losses in the sample. It is now possible, also by computation, to make allowance for, and even to eliminate the corruption of the image by spherical aberration, and of chromatic aberration with the aid of computation or energy-filtering.[26] In practice, as explained[4] elsewhere, a convenient operational procedure in HRTEM is to record a series of images at a series of settings of lens defocus and as a function of sample thickness. By comparing an observed image with that computed through the well-proven so-called 'multi-slice' procedure (for the conditions that apply in the imaging), a trustworthy result is obtained. Urban *et al.*,[27] in an electron microscopic *tour de force*, using a 200 keV instrument so designed as to operate with a point resolution of 1.3 Å, invoked the multi-slice method to resolve individual columns of oxygen atoms in $SrTiO_3$.

With the availability of slow-scan CCD cameras and the recent digital revolution, it is now possible to treat the digital data of electron diffraction patterns and the corresponding HRTEM images recorded under low-dose conditions in a quantitatively rigorous

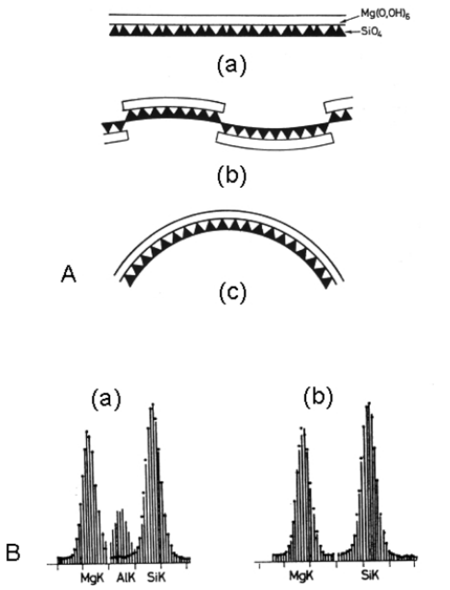

Fig. 6 Many mineralogists had suggested that the supposed microstructure of the three polymorphs of serpentine (see text) are as shown in A: (a) lizardite, (b) antigorite, and (c) chrystotile with substitution of Al for Mg ions in octahedral sites and/or Al for Si ions in tetrahedral sites. Combined HRTEM and X-ray emission spectroscopy (XRE) (B) showed that antigorite and chrysotile are compositionally identical—neither of them contains Al—but the flat lizardite does have the dimensions of the octahedral sheets which explains why they equalise those of the tetrahedral ones.[25] Antigorite is seen, by HREM, to be a modulated structure. Reproduced with permission from The Royal Society of Chemistry.

manner. Provided the precise experimental conditions (crystal thickness, degree of electron-beam tilt to the crystallographic axes and extent of defocus of the objective lens) are known, one may solve the crystal structure using electron crystallography. A high-resolution (HR) electron micrograph (of an ultra-thin specimen) contains all the required information (*i.e*. the relative phases and the amplitudes of the diffracted beams) for an *ab initio* solution of the crystal structure. Terasaki, who has pioneered this method, takes a (computed) Fourier diffractogram of the HR image, recorded down several zone axes. It has proved particularly helpful in solving the structure of mesoporous silicas (such as SBA-6[28]) and also of zeolites. Independently, Gonzalez-Calbet *et al.*,[29] used electron crystallography to solve the structure of zeolite MCM-22..

So, in summary, there are two ways in which the atomic structure of a solid (not amenable to attack by conventional X-ray means) may be solved by HRTEM:

(i) the 'multi-slice' approach, which matches computed images based on a plausible trial structure, projected along high-symmetry directions, with corresponding HRTEM images recorded under well-defined conditions of thickness, defocus, spherical aberration of lens; and

(ii) the electron-crystallographic approach, which is effectively the analogue of the direct methods approach in X-ray crystallography.

Both these methods are in current use, but the electron-crystallographic method did not come into its own until the advent of the slow-scan CCD. An earlier, and highly effective, variant of the electron crystallographic approach was first used by Klug for determining the structures of viruses and other materials in molecular biology.[30] Henderson's classic determination of the structure of the purple membrane was done using this method, as was Unwin's recent determination of the structure of acetylcholine. This entailed using the amplitudes from the intensities of the electron-diffraction spots and the extraction of the phases of the corresponding reflections from the high-resolution image. (Phases are more important for solving the structure, while amplitudes are more important for refining it. As long as the phases are correct, errors in the amplitudes do not materially change the atomic positions.) Zewail and co-workers have very recently[31] introduced a new technique, called 'ultrafast electron crystallography' which is capable of determining distances between atoms at a solid surface with a resolution of *ca.* 0.05 Å parallel to the surface and *ca.* 0.02 Å perpendicular to it. Their technique has the added advantage of probing transient structures.

The 'Klug' method (which has the great advantage of being able to cope with as little as 10^4 unit cells) has not been applied routinely to the solution of inorganic structures, with a few notable exceptions. It has been used by Hovmöller[32] on some complex oxides and chalcogenides.

The 'multi-slice' approach has had numerous successes, including the solution of structures of many synthetic zeolites. A particularly interesting example concerned the relatively rare mineral rhodizite[32] (composition $(K_{0.44}Cs_{0.36}Rb_{0.07})B_{11.3}Be_{4.5}\cdot Al_4O_{28}$), which, besides being one of the hardest solids known, is extremely insoluble in most solvents. Very few chemical clues were therefore available for its structural elucidation. By taking HRTEM images along the three-principal directions, the essential features of the structure, which was refined by supplementary information (high-resolution solid-state MAS NMR spectra and EELS data—see below) were determined.[33]

La_2CuO_4, like many other oxide ceramics, is a very good warm superconductor. Many of these so-called cuprate ceramics consist of La, Y, Bi and Tl and have the general formula $(AO)_n(BCuO_{3-x})_m$, where n and m correspond to the intergrowths of rock salt (AO) type layers and oxygen deficient perovskite ($BCuO_{3-x}$) type layers, respectively. Electron microscopy, especially HRTEM, has played a crucial role in determining the local structure and chemical consequences involving oxygen vacancy (anion) ordering, stoichiometric variation, structural modulations, substitutional defects, oxygen interstitials, grain boundary interfaces and coherent intergrowths which have been found to play a profound role in governing charge-carrier concentrations, critical currents, flux pinning and other features that influence the practical performance of superconducting devices.[34]

In regard to La_2CuO_4, and many similar materials, there is doubt as to whether its surface structure (and that of similar ternary and quaternary oxides) is the same as that of the bulk solid. HRTEM has the advantage over scanning tunnelling and atomic force microscopy in being able, through the observation of parallel X-ray emission spectra, to yield elemental composition. When a strictly stoichiometric powdered sample of La_2CuO_4 was viewed down the [110] direction by HRTEM, the resulting image of the ternary oxide surface was as shown in Fig. 7. The composition clearly does not correspond to La_2CuO_4. Images such as that in Fig. 7 leave no doubt (and microanalysis confirms it) that the exterior surfaces—

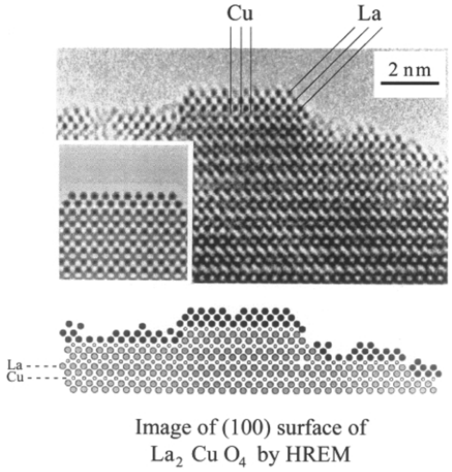

Fig. 7 The outer layers of the surface of La_2CuO_4 (viewed down [110]) are seen by combined HRTEM and XRE to have the structure and composition of La_2O_3, a feature common to other (superconducting) complex perovskite oxides. Reprinted from *Curr. Opin. Solid State Mater. Sci.*, **5**, W. Zhou and J. M. Thomas, "HRTEM surface profile imaging of solids", p. 75, Copyright 2001, with permission from Elsevier.

the last three or so layers—have the so-called C-La_2O_3 structure and composition.[35] The warm superconductor $HgBa_2CuO_{4+\delta}$ is likewise, at its surface, very different in structure and composition from its bulk.[36] Evidently these materials undergo extensive surface reconstruction and reconstitution, a fact that has profound implications in their technological application. This example emphasises the dangers of relying solely on STM or AFM images, where no means exist to record the composition of the surface layers.

Many structures of important inorganic materials have been solved by the HRTEM-multi-slice computation method. For example, the centrally important so-called pentasil zeolite, ZSM-5, for a long time defied all attempts to crystallise into specimens sufficiently large to permit of single-crystal X-ray analysis. Powder X-ray diffraction did provide a skeletal outline of the open structure and this enabled one of us (J. M. Thomas) to reveal[37] in graphic fashion high-resolution images of ZSM-5 (Fig. 8). HRTEM also revealed that an infinitely large family of sub-unit cell intergrowth structures of ZSM-5 and ZSM-11 could exist (see Fig. 8(b)). In addition, it provided direct, real-space evidence and proof that the new pentasil zeolite designated ZSM-23 is a recurrently twinned version of the related zeolite theta-1,[38] whose structure was also solved initially by a combination of electron diffraction, HRTEM and X-ray powder diffractometry.

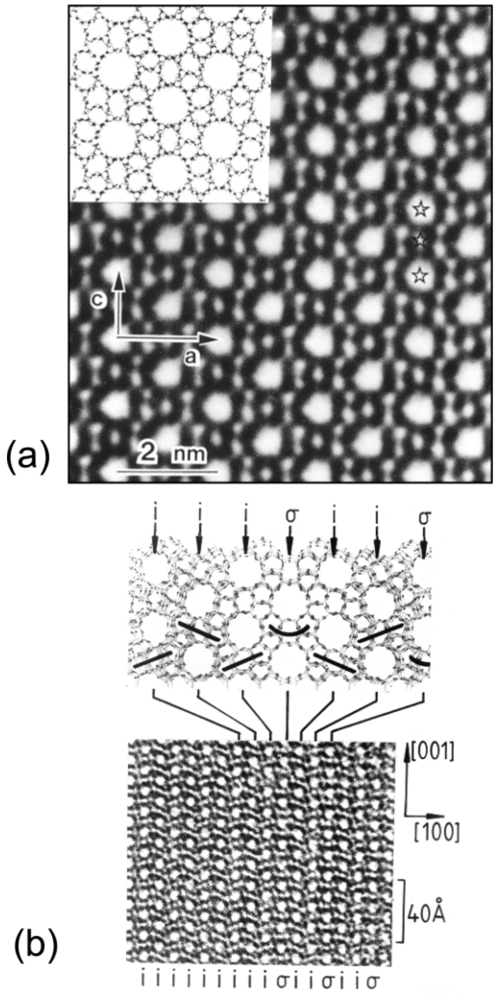

Fig. 8 (a) HRTEM, with associated structure projection drawing (down [010]) of zeolite ZSM-5;[37] (b) Regions of the related structure, ZSM-11, here designated s, tend to intergrow within regions of ZSM-5 (designated *i*). Reproduced with permission from The Royal Society of Chemistry.

In similar vein, Leonowitz and Vaughan used HRTEM to propose a structure for their synthesised zeolitic catalyst (very important in petrochemical contexts) ECR-1.[39] The structure is an intimate twin of the mordenite and mazzite structures, two naturally occurring zeolites. One of us and his colleagues uncovered[40] hitherto unrecognised stacking relationships in whole families of zeolites (such as the so-called ABC-6 family); and they discovered by HRTEM a bizarre coincidence boundary in the zeolite-L (Fig. 9).[41] Such unusual structural faults are not simply of academic interest. It so happens that zeolite-L is the basis of a commercially important industrial catalyst that converts certain alkanes to benzene.[42] The performance of such catalysts is greatly impaired, if they contain just a few of these coincidence boundaries because the diffusivity of the reactant alkane is greatly diminished as a result of the severe blockage introduced into the structure by such boundaries.

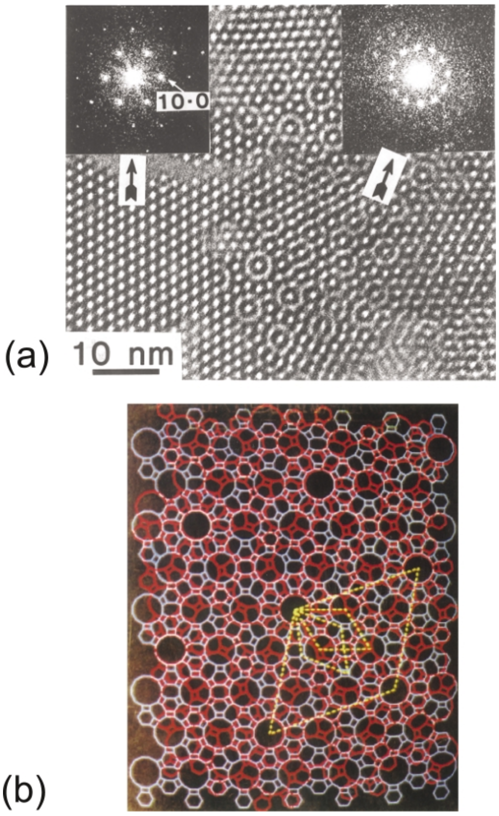

Fig. 9 (a) HRTEM image of zeolite L. The left part shows the arrangement of main channels (diam. 7.4 Å), and the optical diffractogram of this region (above) shows the expected six {10.0} reflections. The right part of the image shows the $\sqrt{13}.\sqrt{13}R32.2^\circ$ superlattice repeats, and its optical diffractogram has twelve-fold symmetry. As a result of the occurrence of just one such coincidence boundary, because of the blockage of channels, the number of primary tunnels is reduced to *ca.* 8 per cent of the number in the unfaulted crystal (see (b));[41] (b) Illustration of the $\sqrt{13}\sqrt{13}R32.2^\circ$ superlattice. Reproduced with permission from The Royal Society of Chemistry.

Many other structures have been solved taking HRTEM images as the starting point for the solution. The extremely important aluminophosphates, No. 36, for example, had defied all attempts by X-ray analysis alone until information concerning the size of its pore apertures (determined by HRTEM) were incorporated into the results of high-resolution powder X-ray diffractometry and electron diffraction patterns.[43] Transition-metal-ions (such as Co^{III} and Mn^{III}) substituted in place of Al^{III} into AlPO-36 convert it to a powerful selective oxidation catalyst for alkanes in air;[44] and when Co^{II}, Mn^{II}, Mg^{II}, Zn^{II} are present substitutionally in this particular framework extremely powerful solid acid catalysts are generated, capable of converting methanol into light olefins.[45]

HRTEM has also proved invaluable in examining the colloidal state of inorganic matter.[46] For example, preparations of colloidal platinum—following the recipe of Michael Faraday (in the 1850s) whose colloidal gold and platinum sols are still in a state of beautiful dispersion as demonstrated by the light scattering of a red laser beam, Fig. 10—and see by HRTEM to exhibit high

Fig. 10 HRTEM shows that, even in individual colloidal particles of metals (such as those prepared (left) by Michael Faraday (top right) in the mid 1850s), there is regularity in the packing of the boundary atoms (as in colloidal Pt) as seen in the two micrographs (bottom right). (After J. M. Thomas, *Nova Acta Leopoldina*, 2003, **88**, 109. Reprinted with permission from the Deutsche Akademie der Naturforscher Leopoldina.)

crystallographic order. Likewise, nanoparticles of colloidal cobalt ferrite ($Co_{.73}Fe_{2.27}O_4$) of diameter in the range 1 to 25nm—which have a number of interesting practical applications as ferrofluids—are found by HRTEM to be of high crystallinity and crystallographically well-defined faces, {022} and {311} being preferred.[47]

Of late, bimetallic nanocatalysts of diameter *ca.* 1.5 nm, such as Ru_6Pd_6, $Ru_{12}Cu_4C_2$, Ru_6Sn and $Ru_{10}Pt_2$ have been found to display exceptionally high catalytic activity and selectivity in the hydrogenation of a number of key organic compounds, particularly those that are relevant to the domain of sustainable development.[48] Such nanoparticle catalysts are supported within the well-defined mesopores (*ca.* 3 nm diameter) of silica; and the key to their preparation involves sequestering the anionic mixed-metal carbonylate in association with an appropriate cation (such as $[PPN]^+$, where PPN stands for bis-(triphenylphosphane)iminium as shown in Fig. 11.[49]

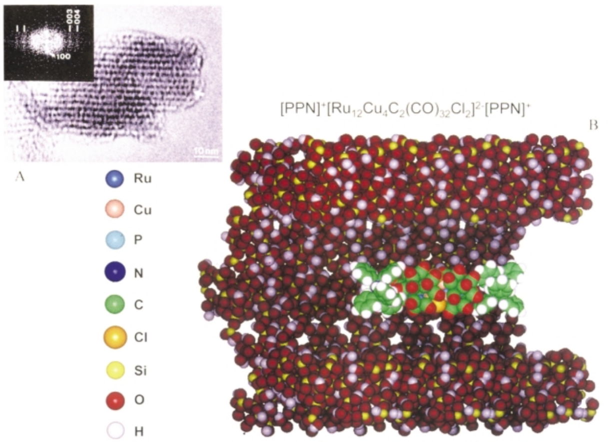

Fig. 11 Colour graphic representation of how readily a mixed metal carbonylate salt (in this case $[Ru_{12}Cu_4C_2(CO)_{32}Cl_2]$ $[PPN]_2^+$—see text) may be incorporated into the pores of a mesoporous silica (13 Å diameter). The electron micrograph (top left), with its associated diffraction pattern (Fourier transform) shows the highly ordered nature of the bulky bimetallic salt within the pores.[49] Reprinted with permission from the Deutsche Akademie der Naturforscher Leopoldina.

HRTEM, with parallel (computed) electron diffraction pattern (*i.e.* the Fourier transform of the image) shows that the precursor ions, in association with their neutralising cations (*e.g.* Ru_{12}-$Cu_4C_2(CO)_{32}Cl_2]^{2-}(PPN)_2^+$) are compactly aligned within the mesopores of the silica.[49] Incorporation of neutral ionic clusters as one-dimensional arrays in single-walled carbon nanotubes, are ideal for study by HRTEM, as the recent work of Kirkland and co-workers[50] has elegantly demonstrated (Fig. 12). Here, the crystallographic repeat distance of the guest is incommensurate with that of the host.

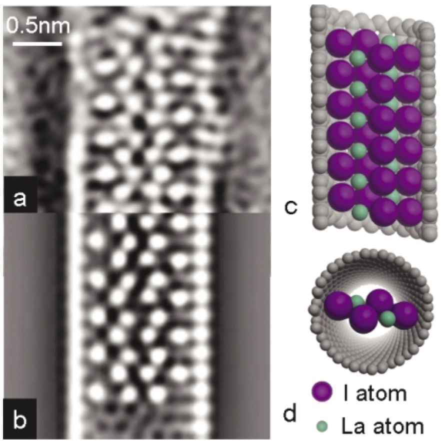

Fig. 12 (a) A high resolution image, reconstructed from a through-focal series of micrographs, of a 'one-dimensional' crystal of LaI_2 encapsulated within a chiral (18,3) single wall carbon nanotube; (b) shows a simulation using a multi-slice calculation of the 'nano-composite' illustrating the excellent match between the experimental positions and intensities of the La and I atoms and the asymmetry in the nanotube wall contrast brought about by the tube's chirality; (c) and (d) are schematic projections of the nano-composite parallel and perpendicular to the tube axis. (Figure courtesy of Dr. S. Friedrichs).

It was HRTEM and associated multi-slice computations that first established that single sheets of graphite, (now very much in the public eye because of the utility as hosts and for other purposes) could be reliably imaged by electron optical methods.[51] HRTEM also showed[5] that single layers of MoS_2 and WS_2 could be readily imaged. Early work[52] done up to the 1980s showed that nanoparticles of metals such as iron (often in association with cabidic phases such as Fe_3C and Fe_5C_2, which could be identified directly from interplanar spacing) could give rise to extensive growth of carbon nanotubes (see Fig. 13), a phenomenon of ancient lineage.[53]

High-resolution scanning transmission electron microscopy (HRSTEM)

Images recorded *via* scanning transmission electron microscopy, formed by a finely focused probe (*ca.* 0.5 nm diameter) have, in general, slightly inferior resolutions compared with analogous HRTEM ones. This is in part because of the finite source size, the scan stability and the reduced detection efficiency imposed by the geometry of the collection of the scattered electrons. But, in two important respects, HRSTEM images have important advantages:

(i) it has ultra-high resolution nano-analytical capabilities of X-ray (and visible light) emission and Auger and electron-energy loss spectroscopy—see next Section—and

(ii) all the signals may be collected simultaneously, together with back-scattered electrons.

Since HRSTEM readily yields high-angle annular dark-field (HAADF) images, as well as bright field (BF) images, formed from the transmitted electrons, and ordinary dark-field (DF) images, formed from Bragg-scattered beams, there are extra benefits to be gained by its use in locating nanoparticles composed of as little as just two- to ten-atom clusters.

A particularly important feature of HRSTEM is so-called Z-contrast imaging[4] (atomic number imaging), which exploits the fact that high-angle scattering intensity of electrons from thin specimens follows the Z^2 dependence of Rutherford's law, where Z is the atomic number. (Just one atom of Pt scatters as strongly as about a 100 atoms of oxygen or 32 atoms of silicon). The technique is

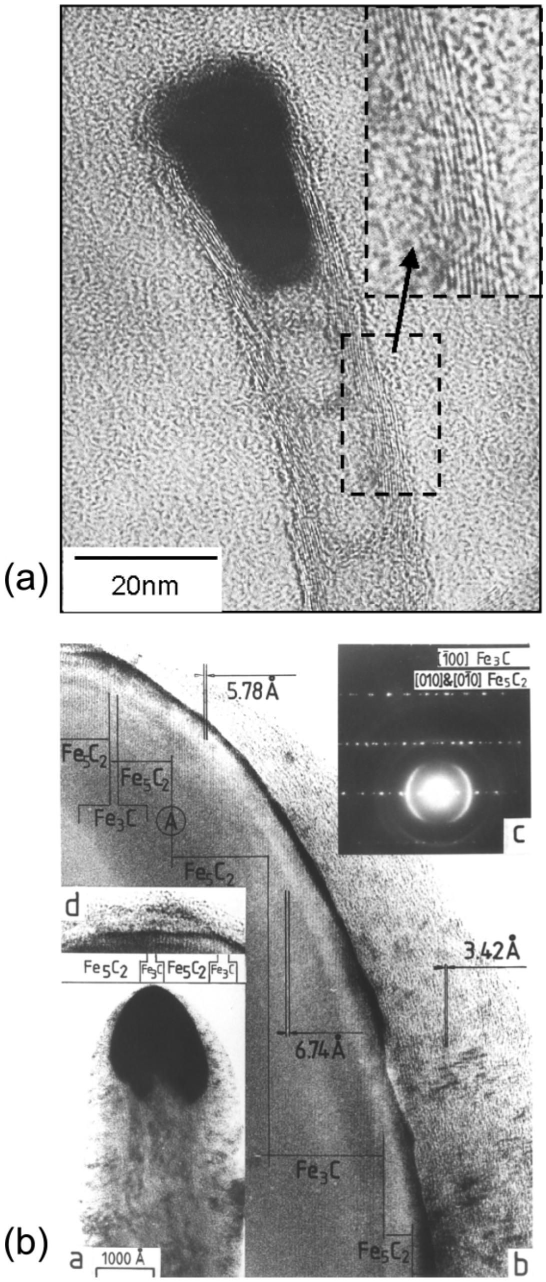

Fig. 13 (a) HRTEM of multiple-walled carbon nanotube (diameter 60 Å) formed by the Fe-catalysed disproporionation of CO. (Audier and Thomas, 1981 unpublished); (b) From the interatomic spacings, determined by HRTEM, two distinct carbide phases (Fe_3C and Fe_5C_2) are identifiable as the templates on which the multiple-walled carbon tube forms. Reprinted from *Ultramicroscopy*, **8**, J. M. Thomas, "Placing the applications of high-resolution electron microscopy to chemical problems into wider perspective", p. 13, Copyright 1982, with permission from Elsevier.[52]

ideally suited for detecting clusters of catalytically active metals or bimetals (such as Ru, Pd, Sn, Cu, etc. described above—see Fig. 14), on light supports such as open-structure silica, zeolites or aluminophosphates. It is also well-suited for element mapping (Fig. 15).

To illustrate the power of HRSTEM, we focus on the twelve-atom nanoparticle catalyst, $Ru_{10}Pt_2$, formed by decarbonylation (by gentle thermolysis—monitored, *in situ*, by FTIR) of the precursor anion (and its associated neutralizing cations PPN^+). Our independent X-ray absorption spectra[47] shows that the individual nanocatalysts are anchored to the mesoporous silica support *via* two Ru–O and one Pt–O covalent linkages (Fig. 16). This catalyst smoothly converts *trans,trans* muconic acid to adipic acid in hydrogen. (It is therefore a key catalyst in the context of sustainable development since the muconic acid is readily preparable, *via* biocatalysis, using

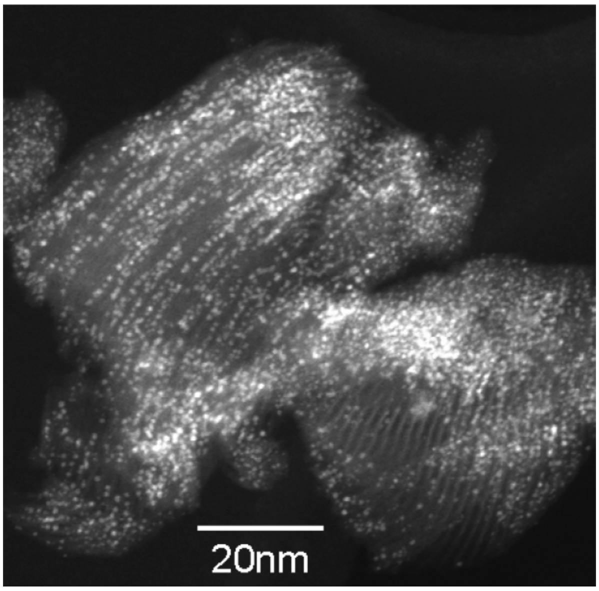

Fig. 14 HRSTEM (High-angle annular dark field (HAADF)) image of Ru_5Pt bimetallic catalysts (mean diameter 15 Å, inside mesoporous silica (diameter 33 Å).

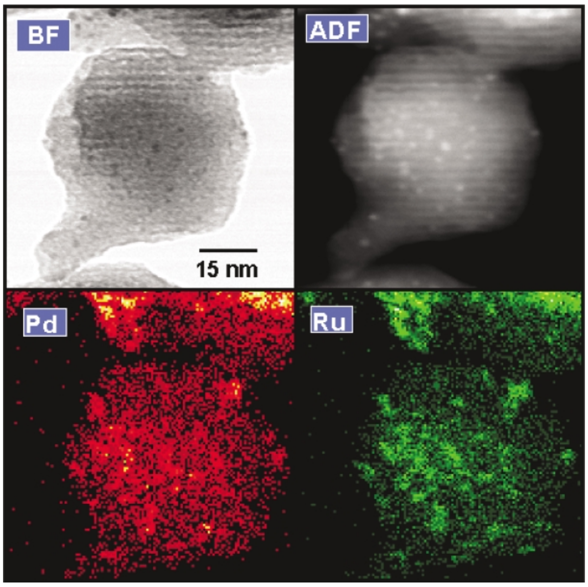

Fig. 15 X-ray element maps (Pd K and Ru K edges) showing that the Ru_6Pd_6 nanoparticles retain their elemental integrity (during and after use as hydrogenation catalysts[48]).

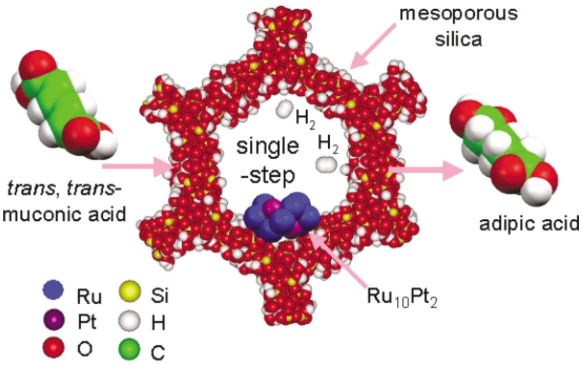

Fig. 16 The bimetallic nanoparticle catalyst $Ru_{10}Pt_2$ anchored *via* two Pt–O and one Ru–O bonds (established[46] by XAFS) converts *trans,trans*-muconic acid (shown at left) in H_2 to adipic acid (right).[54]

the appropriate strain of *E. coli*, from glucose, which, in turn, may be derived from biomass, and adipic acid is a prime component of nylon and other fibres).

Fig. 17 shows a typical view of the HAADF image of this $Ru_{10}Pt_2$-silica supported hydrogenation catalyst. The alignment of the individual nanoparticles inside the 3 nm diameter mesopores, and their freedom from coalescence after use as catalysts, is apparent. The electron-induced emission spectra of each nanoparticle, weighing 2 zeptogram (2×10^{-21}g) shows that the Ru:Pt ratio is 5:1.[54] Numerous comparable studies have recently been published, as have element maps, showing the spatial distribution of the elemental components of the nanocatalyst particles over the support material. Such images, being two-dimensional projection maps, unlike some of the scanning electron tomographs described below, do not reveal the three-dimensional distribution. Neither do they authentically convey the morphology of the nanocatalysts.

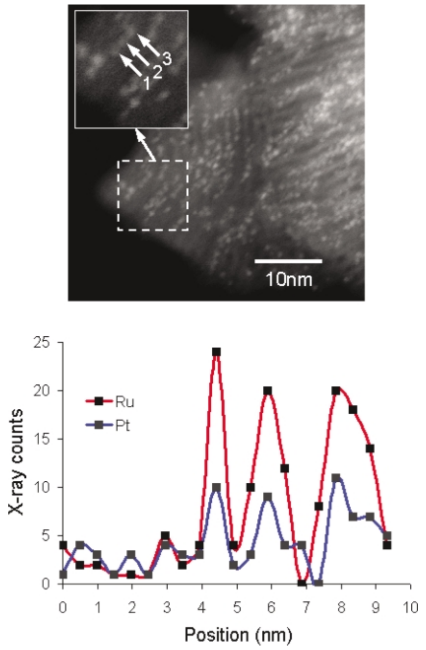

Fig. 17 HRSTEM (HAADF) image of the RuPt nanocatalyst. Inset shows the nanoparticles studied by X-ray emission, the spectra being recorded in spatial sequence approximately every *ca.* 5 Å. From the area under the spectral curve in the region containing the three nanoparticles, the ratio of Ru:Pt for each particle is determined (by appropriate calibration standards) as 5:1, in line with that expected from decarbonylating the precursor $[Ru_{10}Pt_2(CO)_{28}]$ anions.[54]

Electron-energy-loss spectroscopy (EELS)

Both conventional transmission and scanning transmission electron microscopes can be fitted with electron spectrometers, or energy filters, such as to make it possible to study the various energy loss processes that are schematised in Fig. 18.[55]

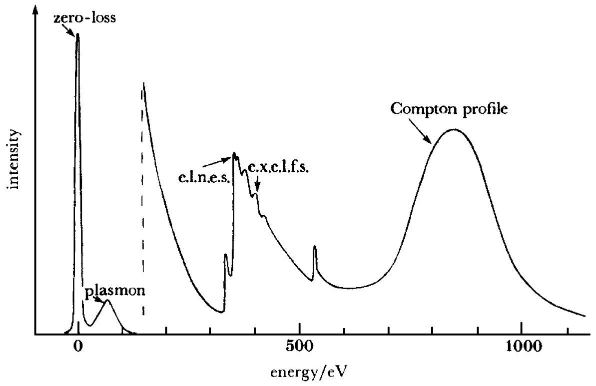

Fig. 18 Schematic diagram of the various possible energy loss processes that may be observed in an electron microscopy.[55]

The range of energies over which we obtain reasonable signals extends to about 2000 eV below the incident energy. The zero-loss peak at the energy of the incident beam, arises partly from those electrons that are scattered elastically in the forward direction, but since the resolution is not sufficient to resolve phonon energies, which are typically of the order of one tenth of an electon volt or less, this also includes thermal diffuse scattering. Proceeding through progressively increasing loss of energy, the first feature of interest is the plasmon peak, and this usually occurs between about 5 and 25 eV. Since plasmons are collective excitations of the electron gas their energies are governed by the density of the electrons in the sample and the extent to which the electrons are free or bound: clearly it is much easier to excite a collective oscillation if the electrons in the sample are free.

At higher energy losses the intensity falls by several orders of magnitude but, if the vertical scale is changed, steps are observed at energies corresponding to the binding energies of the electrons in the sample. These occur at all energies from a few electron volts to hundreds of thousands of electon volts, but since these experiments cover a loss range of about 2ke V, the observed binding energies correspond to the outer 2 or 3 shells of electrons. The point here is that an electron will be excited only when the energy transfer is greater than the binding energy, but that, once this point is reached, there will be an abrupt increase in the scattering cross section. Since the height of the step is proportional to the amount of that element that is present, the edges can be used to determine the chemical composition of the sample, if the cross section from exciting that edge is known (Fig. 19).[5]

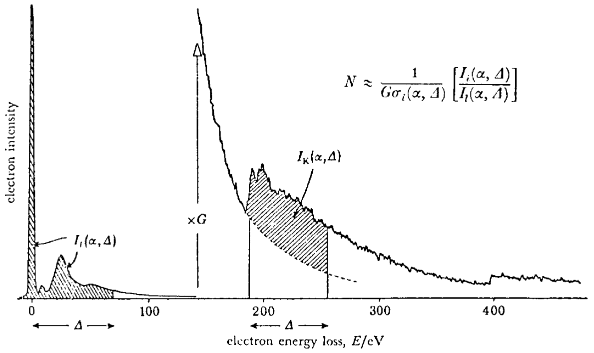

Fig. 19 EEL spectrum of crystalline boron nitride, showing the boron K-edge (at 190 eV) and the nitrogen K-edge (at 400 eV). The background intensity, delineated by the dashed curve arises from inelastic scattering by valence electrons. The hatched areas represent the measured values required for the quantitative analysis of boron. *N* in the equation is the concentration of a measured element in atoms per unit area of specimen, σ is the partial cross-section dependent on the collection angle, α and the integration width Δ. Reprinted with permission from *Inorganic Chemistry: Towards the 21st Century*, A. C. S. Symposium Series 211, 1983, p. 445. Copyright 1983 American Chemical Society.[5,61]

A closer examination of the edge shows that it is not just a simple step, but there is a significant fine-structure. This structure reflects the energy density of unoccupied states in the region of the Fermi energy and provides information relating to the band structure; but it also depends on the core hole that is left behind when an electron is ejected from its ground state, so that exitonic effects must be included in a full description.

Beyond this near-edge structure there is further structure, which is essentially the electron equivalent of X-ray absorption fine structure or XAFS and goes under the abbreviation of e.x.e.l.f.s for extended-energy-loss-fine-structure. This arises from interference effects due to neighbouring atoms when one tries to eject electrons from a particular atom with a wavelength of the order of the nearest-neighbour distance, and therefore yields information about the local coordination of the atom whose edge is under investigation.

Finally, if in addition to all of this, one looks not at the electrons that have been transmitted straight through the sample, but at electrons that have been scattered through an angle of about 5°, one finds the Compton profile. As we shall see, the Compton profile provides[56] a measure of the ground-state momentum wavefunction of the electrons in the sample.

(a) Plasmon scattering

Using a simple classical argument we obtain the well known expression for the frequency of the plasma oscillations in terms of the electron density $\omega = (ne^2/m\varepsilon)^{\frac{1}{2}}$. For the free-electron metals, the conduction electrons may be treated as a Fermi gas, so that the plasmon concept applies quite precisely. One may then derive the expression for the plasma frequency simply by imagining that the sea of electrons is displaced sideways and then released. The restoring force is linear, the oscillation is simple harmonic and the frequency is given by the above equation. Fig. 20 shows a collection of plasmon spectra, which were measured for two free-electron metals, and in each case the plasmon lines, each at an integral multiple of the fundamental plasmon energy to provide a rapid means of identifying these elements in their metallic state.[57]

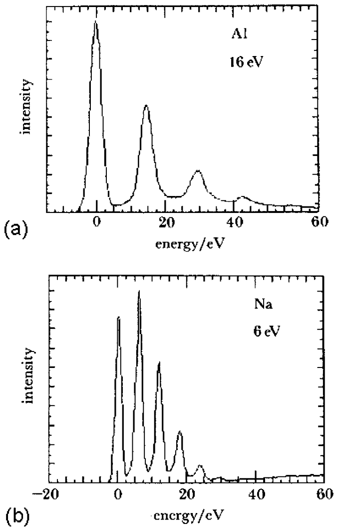

Fig. 20 The identification of minute quantities (*ca.* 10^{-15}g) of metallic Al and Na generated by electron-induced decomposition of their respective hydrides in an electron microscope could readily be made from characteristic plasmon frequencies (16 eV and 6 eV respectively for Al and Na).[57] Reproduced with permission from The Royal Society of Chemistry.

(b) Chemical analysis

The most prominent feature in our schematic energy loss spectrum (Fig. 18) is the edge at an energy transfer corresponding to the binding energy of the core electrons in the sample. We illustrate this with data for BN shown in Fig. 19. As a rule of thumb, one can generally make a quantitative elemental analysis with an accuracy of about 10% and the detection limit is also about 10%, but these numbers do vary greatly, depending on the element one is looking for, as well as on the other elements that are present.

(c) Electron loss near-edge structure (e.l.n.e.s.)

It is clear that there is a certain amount of structure associated with the edges and if we fit, and then subtract, a suitable background this structure stands out more clearly (Fig. 19). E.l.n.e.s. is the electron scattering counterpart of X-ray absorption near-edge structure (XANES). Its occurrence arises, at least in part, from the energy density of unoccupied states. Clearly, a particular transition can take place only if there is an empty state available to accommodate the excited electron, but the structure also depends on the initial state, through the dipole selection rules, and on the interaction between the excited state and the core hole that remains, so that it is necessary to include excitonic effects in a full description. Any transition from a core level to the d-band has a reasonably well defined energy, and this is why sharp lines are observed at transition-metal L edges. In addition to this, the **L** level is split, with the $2p_{1/2}$ and $2p_{3/2}$ levels having different energies so that there are two lines at the edge.

We might expect the intensities of these lines, relative to the shoulder that arises from transitions to the continuum, to increase as the number of empty d-states increases. This is indeed what we find as we go from MnO with five d-electrons in the d-subshell, to MnO_2 with three and then to $KMnO_4$ with none (Fig. 21). The intensities of these lines may therefore be used to estimate the number of d-electrons and hence the oxidation state of elements in compounds of the first-row transition-metal series. Indeed the L_3/L_2 ratio provides a useful probe of the oxidation state of the transition-metal ion. In a recent combined HRTEM/EELS study of ferromagnetism of thin films of Mn-doped ZnO, Sharma *et al.*[58] used the L_3/L_2 (the so-called white-line intensity ration) to find that the Mn was in the +2 oxidation state.

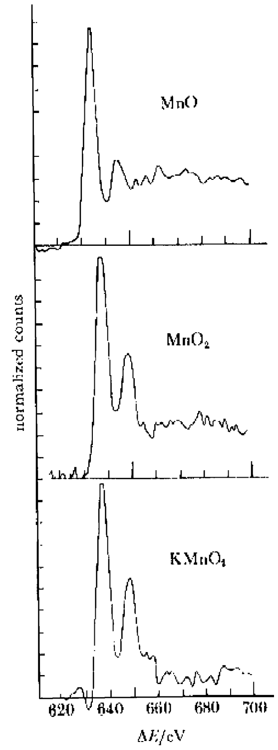

Fig. 21 The number of empty d-states of a transition metal ion is reflected in the L_3/L_2 white-line intensity of the respective EEL spectrum, as seen here for an MnO, MnO_2 and $KMnO_4$.[56]

When a microscrystalline mineral contains many light elements, e.l.n.e.s., proves invaluable as a means of “fingerprinting” the nature of the coordination within the solid.[59] Take again the rather rare minerals rhodizite (see above) and chrysoberyl (Al_2BeO_4). In the former, when one of us (J. M. Thomas) began investigating it, the nature of the coordination of the Al^{3+} and Be^{2+} ions was unknown, but in the latter, X-ray crystallography had unambiguously shown the coordination of these two ions to be octahedral and tetrahedral respectively. The EELS spectra of the Al $L_{2,3}$-edge and the Be K-edge in each of these minerals, as well as the respective computed (multiple-scattering)spectra (using Vvedensky’s IC-XANES code)[60] are shown in Fig. 22, from which it is seen that the e.l.n.e.s. results that, in rhodizite, the Be^{2+} ion is surrounded by a single shell of tetrahedrally coordinated oxygen neighbours and that the Al^{3+} ion has octahedrally coordinated oxygen nearest neighbours. This particular approach prompts confidence in the future possibility of rapid assignment of nearest-neighbour coordinations in complex structures from a database of e.l.n.e.s. fingerprints.[61]

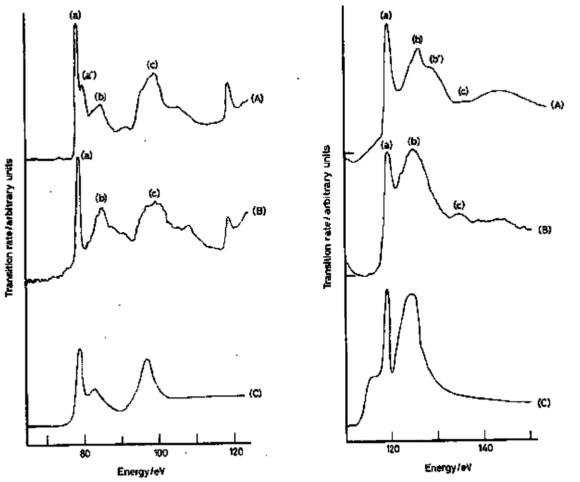

Fig. 22 Left, EEL spectra of the Be K-edge in (A) chrysoberyl and (B) rhodizite after background subtraction. (C) gives the results of computations (see text) for Be^{2+} tetrahedrally coordinated to a single shell of oxygen neighbours; Right, EEL spectra of the Al K-edge in (A) chrysoberyl and (B) rhodizite after background subtraction. (C) gives the computed spectra for Al^{3+} octahedrally surrounded by oxygens.[56] Reproduced with permission from The Royal Society of Chemistry.

(d) Extended-electron-energy loss fine structure (e.x.e.l.f.s.)

The basic idea behind e.x.e.l.f.s. is just the same as in XAFS. The effect is observed when the energy transfer is a little greater than the binding energy of the electrons under consideration. As the ejected electron tries to escape from its parent atom it is scattered by the neighbouring atoms and there will be a tendency for the ejected electron to be reflected back from whence it came. Depending on the wavelength of the electron and the distance to the nearest neighbour atoms, the reflected wave will interfere destructively or constructively with that of the ejected electron. If this interference is destructive the probability of such an event occurring will be diminished, and if it is constructive it will be enhanced. The effect, though weak, leads to an energy loss to be modulated sinusoidally. E.x.e.l.f.s. has never been as successful as XAFS in solid-state chemistry.

(e) Compton scattering

In all the previous subsections of EELS discussed so far it is the energy loss spectrum of the forward scattered electron beam that is under consideration. If, however, the beam is tilted and only those electrons that have then scattered through an angle of about 5° are allowed to enter the spectrometer, an entirely equivalent of the Compton scattering of photons.[56] Such measurements allow us to retrieve the so-called Compton profile, which arises when both the energy and the momentum transfer are large. In essence, what is accomplished in Compton scattering is a measurement of the momentum of the valence electrons in a solid. We use the high energy electrons as probes to evaluate the magnitude of the momentum which, in turn, tells us the nature of the bonding. Thus, even though a thin film of carbon (for example) may be "structureless" using the criteria of SAED, HRTEM (or X-ray diffraction) the nature of the chemical bonding within the film can still be deduced from a profile analysis of scattered electrons. One of us provided proof[55b] from Compton scattering in an electron miscroscope that amorphous carbon is predominantly graphitic.

(f) Element-selective single-atom imaging

As stated earlier ((b) above), EELS is a convenient and highly spatially resolved method of determining elemental compositions of a large variety of materials. Suenaga *et al.*[62] have recently shown that the sensitivity and spatial resolution of EELS can be extended to the single-atom limit. A chemical map of gadolinium (Gd) clearly reveals the distribution of atoms of this element inside a single chain of a single-walled (metallofullerene) Gd@C_{82} as shown in Fig. 23. The fact that the location of individual atoms in nanotubes may be accompanied in this way augurs well for future electron microscopic endeavours in nanoscience and nanotechnology. Another mapping technique is energy-filtered transmission electron microscopy (EFTEM) but the highest resolution achieved to date is ~1 nm and it is unlikely to achieve single-atom sensitivity in the near future.

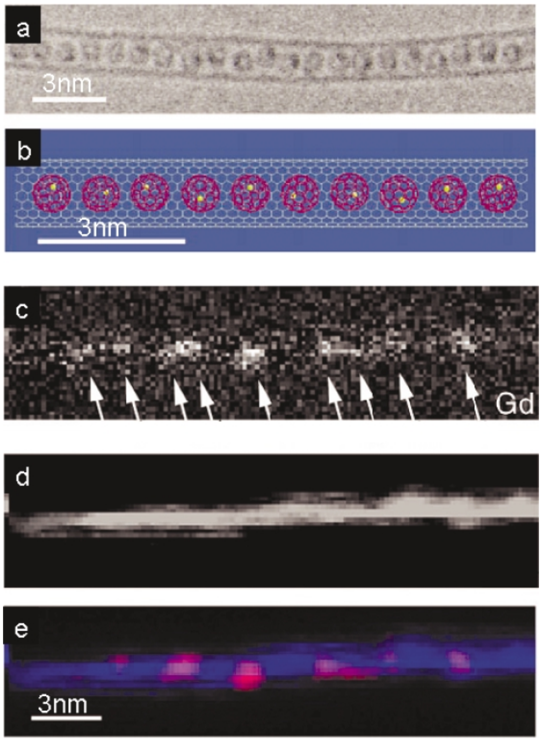

Fig. 23 (a) A high-resolution image and (b) a schematic figure of a chain of endohedral Gd-metallofullerenes (Gd@C_{82}) encapsulated in a single wall carbon nanotube. Gd atoms shown in yellow in (b). Element-selective images using EELS are shown for Gd in (c) for C in (d) and a composite colour image (with Gd red and C blue) is shown in (c). (Intensities of the $GdN_{4,5}$ edge and C K-edge were extracted pixel per pixel from the individual spectra). Reprinted with permission from *Science*, 2000, **290**, 2280. Copyright 2000 AAAS.[62]

Electron tomography

Nowadays, tomography plays a central role in pure and applied science and in most branches of engineering. It entails reconstructing the three-dimensional structure of an object from an angular series of two-dimensional images (projections). We have shown[63] that scanning transmission microscopy in the HAADF imaging mode lends itself admirably to the study of nanoparticle catalysts supported on mesoporous hosts (*e.g.* the $Ru_{10}Pt_2$ bimetallic catalyst on silica shown in Fig. 16 above). Others, notably Baumeister in molecular biological contexts (where cryo-electron microscopic techniques can be used to probe intra-cellular biochemical processes) have used bright-field (BF) electron microscopy as the basis of their electron tomography.[64] BF electron tomography (using conventional transmission electron microscopy) has also shown internal microcavities within zeolitic crystals that were activated prior to their use as catalysts (see Fig. 24).

For inorganic specimens, unlike (unstained) biological structures, there is a large change in both the amplitude and phase of the scattered electron wave, which leads to strong diffraction contrast in a BF image. As a result of this, complications arising from bend contours, thickness contours and Fresnel diffraction will perturb the image contrast and they limit the attainable 3D resolution of the reconstruction, since the image no longer conforms to the projection requirement of electron tomography. As we show elsewhere,[54,63] these problems are greatly minimised by using

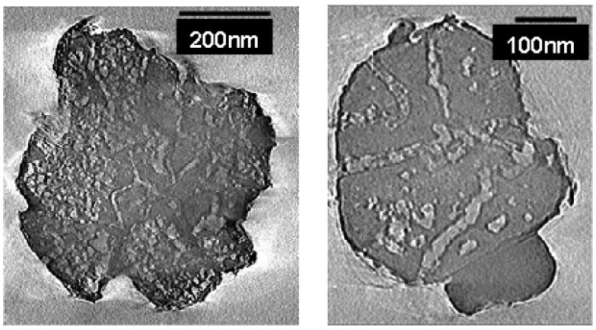

Fig. 24 Bright-field electron tomographs of hydrothermally treated zeolite Y, showing extensive internal pores. After A. H. Janssen, A. J. Koster and K. P. de Jong, *J. Phys. Chem. B*, 2002, **106**, 11905. Reprinted with permission from *J. Phys. Chem. B*. Copyright 2002 American Chemical Society.

STEM and recording HAADF images with electrons scattered to high angles.

We acquired a tilt series of HAADF images from the silica-supported $Ru_{10}Pt_2$ bimetallic catalysts. Fig. 25(a) shows a voxel projection. Also shown (Fig. 25(b)–(d)) are the hexagonal ordering of the mesopores in the silica support, and the clear (colour-coded) locations of the nanoparticle catalysts that are anchored to the walls of the pores. By studying the reconstruction in detail we may extract quantitative data about the distribution of the particle and the pore filling. We may even tell how many nanoparticles are accommodated within each pore, information which, we believe, is impossible to obtain by any other means.

It is not easy to arrive at an accurate value for the 3D resolution seen in the tomographic reconstructions shown in Fig. 25. The pore diameter (*ca.* 3 nm) is well resolved, as are the individual particles (which are 12-atom clusters) known to be less than 1 nm in diameter. We show elsewhere[54] that the attainable resolution is *ca.*1 nm in all three directions.

Tomographic studies by electron microscopy are poised to contribute to many other aspects of the study of surface and bulk features of a wide variety of solids. Great scope exists to explore the detailed topography of solid surfaces and sub-surface regions. Currently available variants of electron microscopy are a far cry from the early, primitive electron microscopic methods in which the simple electron scattering of electrons by “heavy” atoms (such as Au or Ag) were used to decorate topographical irregularities at the exterior surfaces of solids. The decorative technique, introduced by Betghe,[65] and exploited by Thomas,[2,66] was particularly powerful in detecting monoatomic steps at the cleavage faces of alkali halide crystals, and also at the basal faces of oxidised graphite, where individual vacancies could be rendered “visible”. Spiral features (Fig. 26), signifying the unwinding of screw dislocations possessing large Burgers vector (*ca.* 20 nm [001]), as well as atomic steps (0.34 nm) at graphite surfaces revealed a great deal about the role of defects in the oxidizability of graphite and molybdenite (MoS_2). There is no doubt that electron tomography will uncover even more fascinating detail.

In situ electron microscopy

Although the extremely small mean free path of electrons in any gas at atmospheric pressure rules out HRTEM, HRSTEM, EELS and related investigations of solids and their surfaces when exposed to reacting gases or liquid under typical industrial catalytic conditions, remarkable progress has nevertheless been made (especially by Gai[67] and her co-workers) in probing directly, and at the atomic scale, the dynamics of gas–solid, and more recently, liquid–solid, catalytic reactions. This has been done by operating, using specially designed cells, under conditions that closely simulate the real-life conditions, *e.g.*, in the case of vanadyl pyrophosphate (selective oxidation catalyst for converting butane to maleic anhydride) or metal-substituted aluminophosphate (catalyst for the terminal oxidation of linear alkanes) Gai and colleagues operate with the solids exposed to a gas pressure of about 0.1 bar. In this way dynamic *in situ* studies are possible; and novel solid-state transformations (such as shear-glide in vanadyl pyrophosphate)

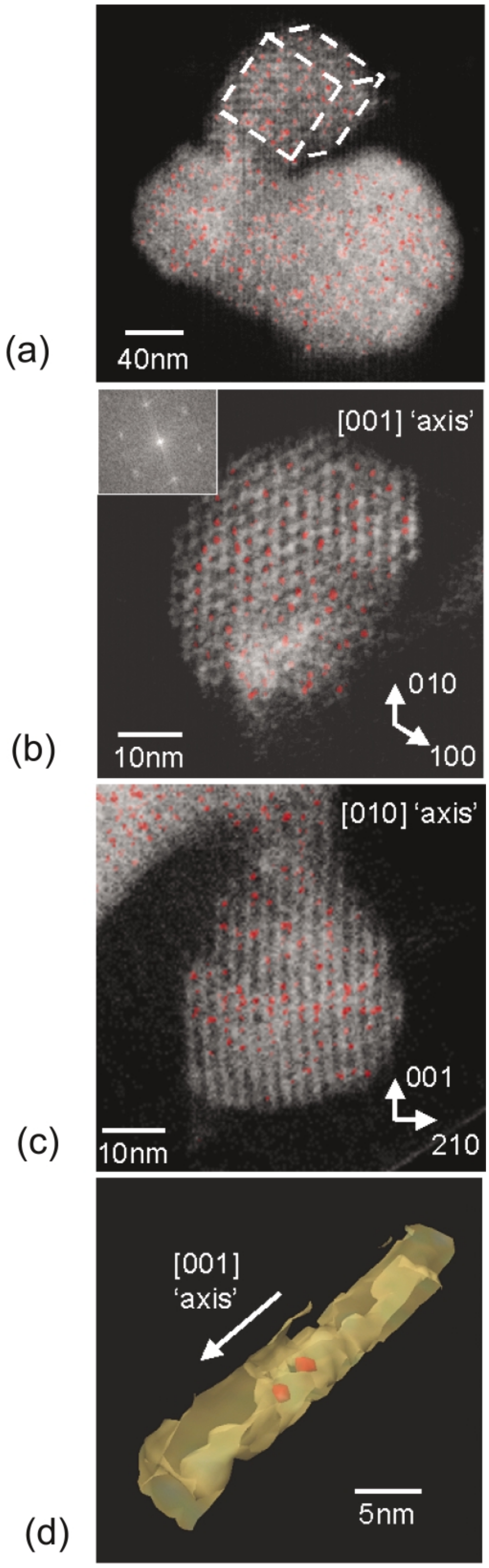

Fig. 25 (a) Perspective view (voxel projection) of a ‘tomographic’ reconstruction of the nanocatalyst $Ru_{10}Pt_2$ supported within a mesoporous framework. Two perpendicular voxel projections (a) and (b) of the reconstruction volume marked in (a). In (b) the hexagonal order of the mesoporous silica is evident (inset shows computed diffraction pattern). In (c) we see the location of the nanoparticles within the pores. (d) is a surface render of a single mesopore extracted (computationally) from the volume to reveal two nanoparticles within its interior.[54]

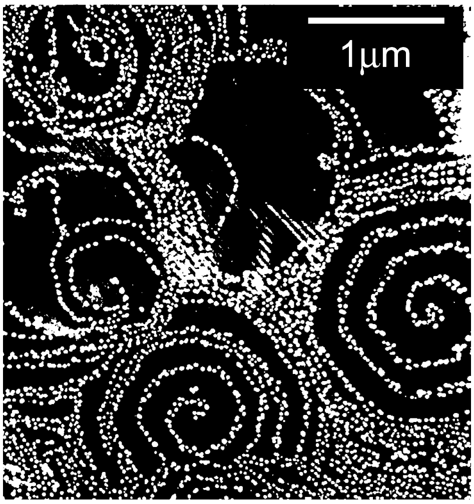

Fig. 26 The occurrence of emergent screw dislocation (of opposite chirality) at the cleaved basal surface of graphite may be rendered visible by the gold-decoration technique, as described in refs. 2 and 66. The preferential growth of gold microcrystals enables step heights of 0.33 nm to be imaged.

have been found to be implicated in the catalytic oxidation of butane.

An environmental TEM cell designed by Gai makes it possible to follow structural changes in Co–Ru nanocatalysts (supported on titania) during their laboratory use (at *ca.* 190°C) in the catalytic hydrogenation of aliphatic dinitriles such as adipodinitrile to hexamethylene diamine (an intermediate in the manufacture of nylon and other polyamides).

Notwithstanding the fundamental problems that prevent *in situ* electron microscopic studies at high pressures, the kind of progress achieved by Gai *et al.*[67,68] and by Danish workers[69] suggests that this approach is likely to yield greater mechanistic insights than atomic force microscopy (which is incapable of elemental analysis) and which, until very recently, lacks the rapidity in operation required for useful time-resolved studies. An impressive illustration of the power of *in situ* electron microscopy is the recent atomic-scale imaging of the growth of carbon nanofibres on nanocrystals of nickel.[70] AFM is, however, fully capable of working under high pressure-high temperature conditions, and also when the solid is submerged in liquid. The very recent work of Humphris *et al.*,[71] who have introduced resonant-scanning AFM, thereby increasing the rate of data acquisition by a factor of over 10^4 promises considerable scope in the future study of surface phenomena such as those reported on zeolites by Agger *et al.*[72]

Notes and references

1 J. M. Thomas, E. L. Evans, B. Bach and J. L. Jenkins, *Nature (London) Phys. Sci.*, 1972, **235**, 126.

2 J. M. Thomas, E. L. Evans and J. O. Williams, *Proc. R. Soc. London, Ser. A*, 1972, **331**, 417.

3 J. G. Allpress and J. V. Sanders, *J. Appl. Cryst.*, 1973, **6**, 165; E. L. Evans, J. M. Thomas and R. J. M. Griffiths, *Science*, 1971, **171**, 174.

4 J. M. Thomas, O. Terasaki, P. L. Gai, W. Zhou and J. M. Calbet-Gonzalez, *Acc. Chem. Res.*, 2001, **34**, 583; see also *Electron Microscopy and the Characterisation of Heterogeneous Catalysis,* ed. P. L. Gai and J. M. Thomas, *Top. Catal.*, 2002, **Vol. 21** and P. L. Gai and E. D. Boyes *Electron Microscopy in Heterogeneous Catalysis*, IOP, Bristol, 2003; J. C. H. Spence, *Experimental High Resolution Electron Microscopy*, OUP, New York, 1988; A. Howie, *J. Microsc.*, 1979, **177**, 1.

5 J. M. Thomas, *Inorganic Chemistry: Towards the 21st Century*, A. C. S. Symp. Series 211, ed. M. H. Chisholm, 1983, pp. 445–471, see also ref. 52 below.

6 G. M. Parkinson, M. J. Goringe, S. Ramdas, J. O. Williams and J. M. Thomas, *J. Chem. Soc., Chem. Commun.*, 1978, 134.

7 C. M. Gramaccioli, G. Filippini, M. Sinnonetta, S. Ramdas, G. Parkinson and J. M. Thomas, *J. Chem. Soc., Faraday Trans. 2*, 1980, 1336.

8 J. M. Thomas and J. O. Williams, *J. Chem. Soc. D*, 1967, 432.

9 J. M. Thomas, *Philos. Trans. R. Soc. London, Ser. A*, 1974, **277**, 251.

10 A. Reller, D. A. Jefferson, J. M. Thomas, R. A. Beyerlein and K. R. Poeppelmeier, *J. Chem. Soc., Chem. Commun.*, 1982, 1378.

11 M. A. Franco, J. M. Thomas and R. D. Shannon, *J. Solid State Chem.*, 1974, **9**, 261.

12 W. Zhou, D. A. Jefferson, M. Alario-Franco and J. M. Thomas, *J. Phys. Chem.*, 1987, **91**, 512.

13 D. J. Buttrey, D. A. Jefferson and J. M. Thomas, *Philos. Mag.*, 1986, **53**, 897.

14 P. A. Midgley and M. Saunders, *Contemp. Phys.*, 1996, **37**, 441. http://www.tandf.co.uk.

15 P. A. Midgley, M. W. Sleight and R. Vincent, *J. Solid State Chem.*, 1996, **124**, 132.

16 E. L. Evans and J. M. Thomas, *J. Solid State Chem.*, 1975, **14**, 99.

17 J. S. Anderson, in Surface and Defect Properties of Solids, *Chem. Soc. Spec. Publ.*, 1972, **1**, 1.

18 M. Alario Franco, J. L. Hutchison, D. A. Jefferson and J. M. Thomas, *Nature*, 1977, **266**, 520.

19 L. A. Bursill, E. A. Lodge and J. M. Thomas, *Nature*, 1980, **286**, 111.

20 J. M. Thomas, M. Audier and J. Klinowski, *J. Chem. Soc., Chem. Commun.*, 1981, 1221.

21 C. N. R. Rao and J. M. Thomas, *Acc. Chem. Res.*, 1985, **18**, 113.

22 D. A. Jefferson and J. M. Thomas, *J. Chem. Soc., Chem. Commun.*, 1980, 743,see also C. R. A. Catlow, J. M. Thomas, D. A. Jefferson and S. C. Parker, *Nature*, 1982, **295**, 658.

23 L. G. Mallinson, J. L. Hutchinson, D. A. Jefferson and J. M. Thomas, *J. Chem. Soc., Chem. Commun.*, 1977, 910, see also J. M. Thomas, D. A. Jefferson, L. G. Mallinson, D. J. Smith and E. S. Crawford, *Chem. Scr.*, 1978/9, **14**, 167.

24 W. Shu-lin, D. A. Jefferson and J. M. Thomas, *J. Chem. Soc., Chem. Commun.*, 1982, 320.

25 E. S. Crawford, D. A. Jefferson, J. M. Thomas and A. C. Bishop, *J. Chem. Soc., Chem. Commun.*, 1978, 986.

26 J. M. Thomas and W. Zhou, *Chem. Phys. Chem.*, 2003, **4**, 927.

27 C. L. Jai, M. Lentzen and K. Urban, *Science*, 2003, **299**, 870.

28 S. Che, Y. Sakamoto, O. Terasaki and T. Tatsumi, *Chem. Mater.*, 2001, **13**, 2237; O. Terasaki and T. Ohsuna, *Top. Catal.*, 2003, **24**, 13.

29 S. Nicolopoulos, J. M. Gonzalez-Calbet, M. Vallet-Regi, A. Corma, C. Connell, J. M. Guil and J. Perez-Paniente, *J. Am. Chem. Soc.*, 1995, **177**, 8947.

30 A. Klug, Nobel Prize Lecture, Nobel Foundation, Stockholm, 1982, 93.

31 (*a*) C.-Y. Ruan, F. Viliotti, V. A. Lobastov, S. Chen and A. H. Zewail, *Proc. Natl. Acad. Sci., USA*, 2004, **101**, 1123; (*b*) J. M. Thomas, *Angew. Chem., Int. Ed.*, 2004, **43**, (in press).

32 S. Hovmoeller, *Ultramicroscopy*, 1992, **41**, 121.

33 A. Pring, D. A. Jefferson and J. M. Thomas, *J. Chem. Soc., Chem. Commun.*, 1983, 734.

34 P. L. Gai and J. M. Thomas, *Supercond. Rev.*, 1992, **1**, 1.

35 (*a*) W. Zhou, D. A. Jefferson and W. Y. Liang, *Surf. Sci.*, 1994, **310**, 52; (*b*) J. M. Thomas, *Stud. Surf. Sci. Catal.*, 2001, **140**, 1.

36 W. Zhou and J. M. Thomas, *Curr. Opin. Solid State Surf. Sci.*, 2001, **5**, 75.

37 (*a*) J. M. Thomas and G. R. Millward, *J. Chem. Soc., Chem. Commun.*, 1982, 1380; (*b*) O. Terasaki, J. M. Thomas, D. Watanabe and G. R. Millward, *Chem. Mater.*, 1989, **1**, 158.

38 J. M. Thomas, G. R. Millward, D. White and S. Ramdas, *Chem. Commun.*, 1998, 434.

39 M. E. Leonowitz and D. E. W. Vaughan, *Nature*, 1987, **329**, 819.

40 G. R. Millward, S. Ramdas and J. M. Thomas, *Philos. Trans. R. Soc. London, Ser. A*, 1985, **399**, 57.

41 O. Terasaki, S. Ramdas and J. M. Thomas, *J. Chem. Soc., Chem. Commun.*, 1984, 216. The picture portrayed by the authors of this article (see Fig. 9(b)) has been used (without permission) as the illustrative cover of a Greek textbook for school children.

42 J. Bernard, *Proc. Naples Conf. On Zeolites*, 1980, Butterworths, p. 628.

43 P. A. Wright, S. Natarajan, J. M. Thomas, R. G. Bell, P. L. Gai, R. H. Jones and J. Chen, *Angew. Chem., Int. Ed. Engl.*, 1992, **31**, 1472.

44 J. M. Thomas and R. Raja, *Chem. Commun.*, 2001, 675.

45 J. Chen and J. M. Thomas, *Chem. Commun.*, 1994, 603.

46 J. M. Thomas, *Pure Appl. Chem.*, 1988, **60**, 1517.

47 J. L. Tirado, J. M. Thomas, D. A. Jefferson, G. R. Millward and S. W. Charles, *J. Chem. Soc., Chem. Commun.*, 1987, 365.

48 J. M. Thomas, R. Raja, T. O'Connell, B. F. G. Johnson and G. Sankar, *Chem. Commun.*, 2003; see also*Science*, (from the Editor's desk),, 9 May,)2003.

49 (*a*) J. M. Thomas, B. F. G. Johnson, R. Raja, G. Sankar and P. A. Midgley, *Acc. Chem. Res.*, 2003, **36**, 20; (*b*) W. Zhou, J. M. Thomas, D. S. Shephard, B. F. G. Johnson, T. Maschmeyer, D. Ozkaya, R. G. Bell and Q. Ge, *Science*, 1998, **280**, 705.

50 A. I. Kirkland and J. Sloan, *Top.Catal.*, 2002, **21**, 139.

51 G. R. Millward, J. M. Thomas and D. A. Jefferson, *Acta Crystallogr.*, 1976, **A32**, 823.

52 J. M. Thomas, *Ultramicroscopy*, 1982, **8**, 13.

53 See, *e.g*. J. M. Thomas and P. L. Walker Jr., *Carbon*, 1970, **8**, 103 and references therein.

54 P. A. Midgley, J. M. Thomas, M. A. Weyland, L. Lafonte, R. Raja, B. F. G. Johnson and T. Khimyak, *J. Phys. Chem. B*, 2004, **108**, 4590.

55 (*a*) J. M. Thomas, B. G. Williams and T. G. Sparrow, *Acc. Chem. Res.*, 1985, **18**, 324; (*b*) B. G. Williams and J. M. Thomas, *Int. Rev. Phys. Chem.*, 1983, **3**, 99; (*c*) B. G. Williams, T. G. Sparrow and J. M. Thomas, *J. Chem. Soc., Chem. Commun.*, 1983, 1434.

56 B. G. Williams, J. M. Thomas and T. G. Sparrow, *J. Chem. Soc., Chem. Commun.*, 1983, 1434.

57 T. G. Sparrow, B. G. Williams, J. M. Thomas, W. Jones, P. J. Herley and D. A. Jefferson, *J. Chem. Soc., Chem. Commun.*, 1983, 1432.

58 P. Sharma, A. Gupta, K. V. Rao, F. J. Owens, R. Sharma, R. Ahuja, J. M. O. Guillen, B. Johansson and G. A. Gehring, *Nature Materials*, 2003, **2**, 673.

59 R. D. Brydson, H. Saver, W. Ergel, J. M. Thomas and E. Zeitler, *J. Chem. Soc., Chem. Commun.*, 1989, 1010.

60 D. D. Vvedensky and J. B. Pendry, *Comput. Phys. Commun.*, 1986, **40**, 421.

61 R. F. Egerton, *EELS in the Electron Microscope*, 1996, Plenum, New York, 2nd Edn.

62 K. Suenaga, M. Tence, C. Mory, C. Collier, H. Kato, T. Okazaki, S. Bandow and S. Iijuma, *Science*, 2000, **290**, 2280.

63 P. A. Midgley, J. M. Thomas, M. Weyland and B. F. G. Johnson, *Chem. Commun.*, 2001, 907.

64 O. Medalia, I. Weber, A. S. Frangakis, G. Gerisch and W. Baumeister, *Science*, 2002, **298**, 1209.

65 H. Betge and V. Schmidt, *Discuss. Faraday Soc.*, 1964, **38**, 79.

66 O. P. Bahl, E. L. Evans and J. M. Thomas, *Proc. R. Soc. London, Ser. A*, 1968, **306**, 53.

67 P. L. Gai, *Top. Catal.*, 2002, **21**, 161, see also P. L. Gai and K. Kourtakis, *Science*, 1995, **267**, 661.

68 P. L. Gai and J. M. Thomas, *Adv. Catal.*, 2004, in press.

69 P. L. Hansen, J. B. Wagner, S. Helvig, J. R. Rostrup-Nielsen, B. J. Clausen and H. Topsøe, *Science*, 2002, **295**, 2053.

70 S. Helveg, C. López-Cartes, J. Sehested, P. L. Hansen, B. S. Clausen, J. R. Rostrup-Nielsen, F. Abild-Pedersen and J. K. Nørskov, *Nature*, 2004, **427**, 426.

71 A. D. L. Humphries, J. K. Hobbs and M. J. Miles, *Appl. Phys. Lett.*, 2003, **83**, 6.

72 J. R. Agger, N. Hasif and M. W. Anderson, *Angew. Chem., Int. Ed.*, 2001, **40**, 465.

73 A. Carlsson, M. Kaneda, Y. Sakamoto, O. Terasaki, R. Ryoo and S. H. Joo, *J. Electron Microsc.*, 1999, **48**, 795.

74 S Che, Y. Sakamoto, O. Terasaki and T. Tatsumi, *Chem. Mater.*, 2001, 2237.

75 D. A. Jefferson, J. M. Thomas and R. K. Grasselli, *J. Chem. Soc., Chem. Commun.*, 1983, 594.

76 R. Vincent, D. Bird and J. W. Steeds, *Philos. Mag. A*, 1984, **50**, 745.

77 D. Schechtman, I. Blech, D. Gratias and J. W. Cahn, *Phys. Rev. Lett.*, 1984, 1951.

78 O. Terasaki and D. Watanabe, *Am. Inst. Phys. Conf.*, 1979, **53**, 253.

79 O. Terasaki, *J. Phys. Soc. Jpn.*, 1982, **51**, 2159.

80 D. Watanabe and O. Terasaki, *NATO Adv. Sci. Inst. Ser. E*, 1984, **83**, 247.

81 J. A. Wilson, F. J. DiSalvo and S. Mahajan, *Adv. Phys.*, 1975, **24**, 117.

82 J. M. Thomas, L. A. Bursill, R. F. Egerton and S. Pennycook, *J. Chem. Soc., Faraday Trans.*, 1981, **77**, 167.

83 R. D. Brydson, J. Bruley and J. M. Thomas, *Chem. Phys. Lett.*, 1988, **149**, 343.

84 J. S. Anderson and B. G. Hyde, *J. Phys. Chem. Solids*, 1967, **28**, 1393; J. S. Anderson and R. J. D. Tilley, *Surf. Defect Prop. Solids*, 1974, **3**, 1.

85 J. S. Anderson, *J. Chem. Soc., Dalton Trans.*, 1973, 110.

86 S. Iijima and J. G. Allpress, *Acta Crystallogr.*, 1974, **30**, 22.

87 J. M. Thomas, *Microsc. Microanal.*, 2002, **8**, 40.

88 L. Kihlborg, *Chem. Scr.*, 1978, **14**, 187.

89 N. Erdmann, K. R. Poppelmeier and L. D. Marks, *Nature*, 2002, **491**, 55.

90 W. Jones, J. M. Thomas and J. O. Williams, *Philos. Mag.*, 1975, **32**, 1.

91 J. M. Thomas, G. R. Millward, R. F. Schlögl and H. P. Boehm, *Mater. Res. Bull.*, 1980, **15**, 671.